Supplement of Nat. Hazards Earth Syst. Sci., 23, 3169–3183, 2023
https://doi.org/10.5194/nhess-23-3169-2023-supplement

Natural Hazards and Earth System Sciences
Open Access
EGU

Supplement of

Mangrove ecosystem properties regulate high water levels in a river delta

Ignace Pelckmans et al.

Correspondence to: Ignace Pelckmans (ignace.pelckmans@uantwerpen.be)

S1. Delineation of mangroves and channels

The use of satellite-borne remote sensing allowed us to delineate the mangroves and channels from aquaculture ponds, urban areas and surrounding agricultural land. ESA's Sentinel 2 is a collection of multi-spectral optical images which allows calculating the Normalized Difference Vegetation Index (NDVI) at a spatial resolution of 10 m. NDVI ranges from -1 to 1 with values above zero, indicating the presence of vegetation. In our study, mangroves were determined by pixels with a NDVI-value above a threshold value. To determine that value, we randomly selected 50 points in the mangroves and 50 points in other land cover types (e.g. aquaculture ponds, built-up areas, etc.). NDVI at all points in mangroves exceed the value of 0.6 while 49 of 50 in other land cover types did not. Consequently, mangroves were determined as all pixels with a NDVI-value > 0.6. To ensure channel connectivity, we applied a 1-pixel-wide dilation and erosion algorithm (Suppl. Figure 1). Afterwards, the entire domain was visually checked and compared with aerial pictures collected through Google Earth. If needed corrections were applied. Finally, manually delineated data of mangroves and channels for sub areas within our study area were available through ESPOL, and after visual comparison, our NDVI-based results were considered satisfactory.

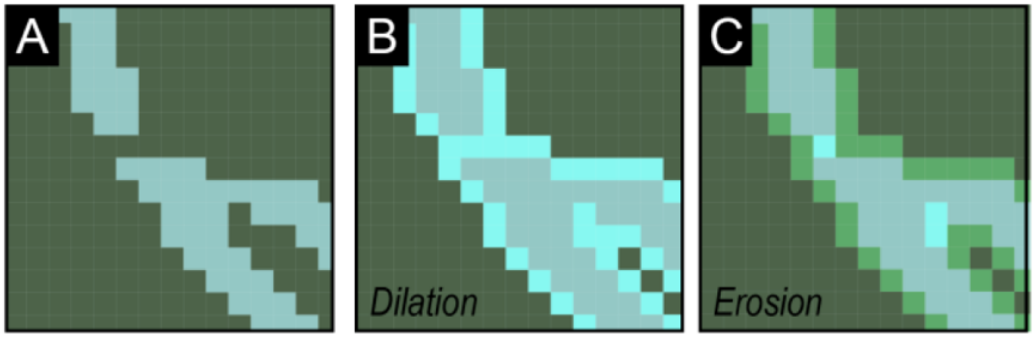

Figure S1 *| Close up of original channel (A) dilation process of 1 pixel wide shown as blue pixels (B) erosion process after dilation, light green pixels indicate pixels which were removed again after erosion (C). Note how the channel kept its original width but is connected now.*

Unrealistic channel bathymetry

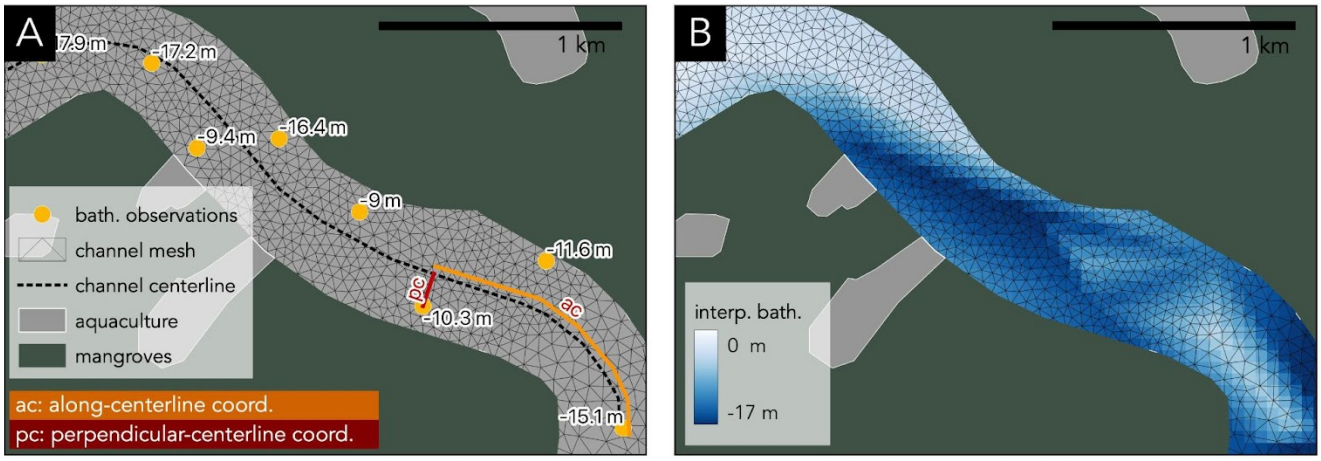

Figure S2 *| Example of channel segment where the distance between bathymetric observations is on average larger than the channel width and indicative example of the along-centerline and perpendicular-centerline coordinates (A) and a resulting interpolated bathymetry using cartesian coordinates (instead of along- and perpendicular-centerline coordinates), which does not conserve the thalweg or bed shape (B).*

S2. Intertidal flat topography

We delineated 20 zones which cover significantly large intertidal flats (area > 40 km2), for which no bathymetric data was available. Per intertidal flat, we collected all available cloud-free Sentinel 2 images through the Google Earth Engine and for each image, the Modified Normalised Difference Water Index (MNDWI) was calculated as:

$$MNDWI = \frac{Green - SWIR}{Green + SWIR} \qquad \text{(eq. S1)}$$

With $Green$ and $SWIR$ being respectively the measured reflectance in the green part of the visible electromagnetic spectrum (560 nm) and short-wave infrared part of the spectrum (1614 nm). $MNDWI$ values range between -1 and +1 with positive values representing open water and negative values representing dry terrain. If the MNDWI in a cell exceeds a threshold value, determined through Otsu-thresholding, the cell can be considered to be submerged, and thus to be located beneath the water surface (Bishop-Taylor et al. 2019). MNDWI values below the threshold are considered to be emerged terrain. The boundary between all emerged and submerged cells (the waterline) is considered then as a contour line with an elevation that is considered equal to the observed water surface elevation at a nearby tide gauge station, measured at the same time as the capture of the Sentinel 2 image. Combining different images, taken at different times and different moments in the tidal cycle, results in a set of contour lines, from which we interpolated an estimated digital elevation model (DEM) of the intertidal flat. Elevation in areas which are located lower than the lowest water level for which a cloud-free image was found, are estimated by linearly interpolating between the lowest found contour line and the surrounding bathymetric data provided by INOCAR, right outside of the intertidal flat. The spatial resolution of the Green and SWIR bands of Sentinel 2 imagery have a spatial resolution of 10 and 20 m respectively. When calculating MNDWI, the resolution of the Green band was aggregated average-based to 20 m and consequently, the eventual spatial resolution of MNDWI was 20 m. As > 99 % of the mesh elements within the intertidal flats have a resolution larger than 20 m, generating the intertidal topography at a spatial resolution of 20 m was considered sufficient.

The waterline-extraction method, as this technique is often referred to, is proven to result in good estimation of intertidal zone topographies. However, it is dependent on the quality and quantity of the available satellite images and on the proximity to the used tide gauge stations (Sagar et al. 2017, Khan et al. 2019).

S3. Discharge extrapolation

The available discharge data only represent 73% of the watershed of the Guayas delta but was completed using a linear precipitation-weighted interpolation with monthly precipitation data collected from OpenLandMap. For each watershed for which discharge data was available, we determined the total precipitation for each month for the period 1990 - 2019 and collected the monthly mean discharge for that respective watershed. The monthly mean discharge was significantly linearly correlated to the total precipitation within that watershed that month (Suppl. Figure 3). We repeated the procedure using daily precipitation sums and daily discharge observations but the resulting linear correlations were weaker than for the monthly series. For each watershed where no discharge data was available, we calculated the monthly total precipitation as well. Next, we estimated monthly mean discharges by applying the linear regression equation from the most nearby discharge-data-available watershed.

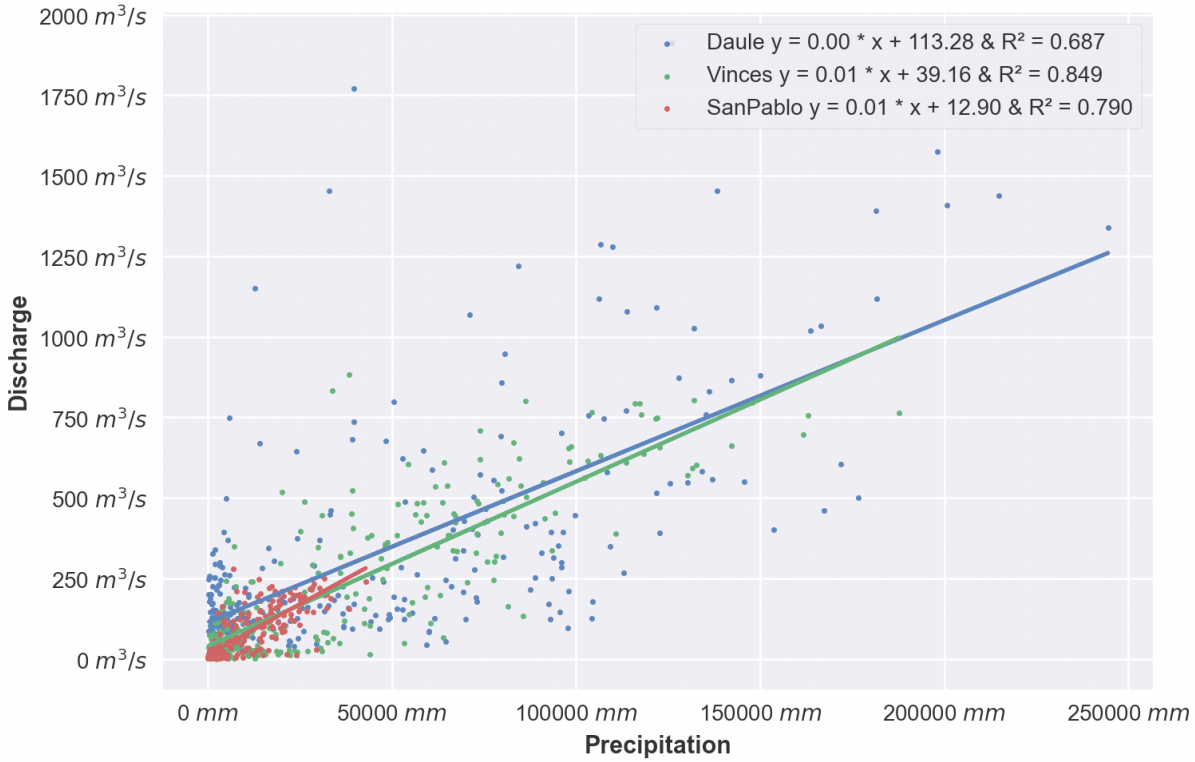

Figure S3 | *Monthly mean discharge values for 3 watersheds plotted againts the total precipitation sums within the respective watersheds. For the three given watersheds, there is a significant linear correlation between precipitation and discharge.*

S4. Vertical reference level

All raw bathymetric data was referenced to local mean sea level (MSL). For 10 of the 11 tide gauges, we know the height of the local MSL relative with respect to the WGS84 reference ellipsoid. These heights were interpolated and added to all bathymetric point observations using a linear TIN interpolation based on the channel coordinates of each bathymetric point relative to the level-I channels. Finally, we reduced the ellipsoidal heights of the bathymetry to a mean-tide quasi-geoid model (mean-tide refers to the adopted permanent tide system, see Mäkinen and Ihde (2009) for more details) that was computed from the XGM2019e geopotential model (Zingerle et al., 2020) on a 2' (appr. 4 km) grid using the service provided by the International Centre for Global Earth Models (Ince et al., 2019). At open sea and along the boundaries, the reduction from local MSL to the XGM2019e-derived quasi-geoid model turned out to be negligible. Note that for our area of interest the quasi-geoid and geoid can be used synonymously.

Bathymetric data in the open sea and the boundary water levels at the seaward boundary did not require corrections as for the seabound tide gauge stations the differences between local MSL and XGM19 reference level are negligible.

S5. Calibration of bottom friction

To calibrate the model, we selected the period of September 22 to October 2, 2019, because (1) for this period we have continuous water level observations from all tide gauge stations, (2) it is the dry season and hence, uncertainties in the river discharge have minimal effect on the calibration process, (3) this period falls outside an El Niño or El Niña event, and (4) it includes a neap tide and a spring tide.

In addition to ME and CRMSE, we also calculated the ratio between standard deviation of simulated water levels and observed water levels ($\sigma_m{}'$, suppl. eq. 4) to assess modelled tidal range and the correlation coefficient R (suppl. eq. 5) to assess model tidal phase:

$$\sigma_m = \sqrt{\frac{\sum_{i=1}^{N}(m_i-\bar{m})^2}{N}} \quad \text{(eq. S2)}$$

$$\sigma_o = \sqrt{\frac{\sum_{i=1}^{N}(o_i-\bar{o})^2}{N}} \quad \text{(eq. S3)}$$

$$\sigma_m{}' = \frac{\sigma_m}{\sigma_o} \quad \text{(eq. S4)}$$

$$R = \frac{1}{\sigma_m * \sigma_o} * \frac{1}{N} * \sum_{i=1}^{N}(m_i - \bar{m})(o_i - \bar{o}) \quad \text{(eq. S5)}$$

where σ_m and σ_o are the standard deviation of the simulated and observed water levels respectively. We compare different simulations on a single Taylor Diagrams polar-coordinate plots which can show $CRMSE'$(normalised CRMSE) and $\sigma_m{}'$ along with R on one single diagram (Kärnä & Baptista, 2016):

$$CRMSE' = \frac{CRMSE}{\sigma_o} \quad \text{(eq. S6)}$$

On such a Taylor diagram, each marker represents the water levels at a tide gauge station and the values on the three axes can be read as follows:

a. the average correspondence between simulated and observed water levels is represented by $CRMSE'$ and can be derived from the diagram as the distance (dashed red lines) of each marker to the reference point (large red marker)
b. $\sigma_m{}'$ indicates the fit between observed and simulated tidal range and can be read on the diagram as the distance (dashed white lines) of the markers to the thick white line. On the latter, the standard deviation of observations and simulations are equal and $\sigma_m{}'$ equal to 1; and
c. the correlation coefficient R is an indicator for the tidal phase performance or the correspondence between the simulated and observed moments in time of high and lower waters. It is shown on a Taylor's diagram as the distance to the dotted blue line where R equals 1.

In Suppl. Figure 4, a Taylor diagram compares simulated water levels with observed water levels at 11 tide gauge stations. For n equal to 0.0175 and n equal 0.0150, tidal phase and mean performance are equally good but the model capacity to represent the tidal range over model domain is significantly better for n equal to 0.0175 (Suppl. Table 1).
While model performance is particularly good in the Western branch, $\sigma_m{}'$ values are increasingly smaller than 1 when the tide propagates upstream through the eastern branch (stations 8, 9 and 11). The model underestimates the tidal range in the eastern channel and fails to capture the upstream tidal amplification (Suppl. Figure 4B). Therefore, we assigned a different Manning coefficient in all channels north and east of tidal station 10, which on its turn was calibrated. A bed roughness of n equal to 0.0125 resulted in the best performance in the eastern branch, according to all evaluation statistics and the Taylor diagram (Suppl. Figure 4C). Changing the Manning coefficient in the eastern branch had no effect on the model performance elsewhere in the domain (Suppl. Figure 4D), and therefore n equal to 0.0175 was kept in the rest of the domain.

Table S1 | *Average (+/- standard deviation) of the following evaluation parameters: Root mean square error (RMSE), standard deviation of the simulated water levels ($\sigma_m{}'$), correlation coefficient (R) and the Nash and Sutcliffe Model Efficiency (ME) for varying Manning coefficient (n) values. The green shaded row indicates the optimal value for the Manning coefficient.*

Manning's n	*RMSE*	$\sigma_m{}'$	*R*	*ME*
n = 0.0125	0.16±0.04	1.13±0.03	0.99±0.01	0.96±0.02

n = 0.0150	0.11±0.03	1.06±0.05	0.99±0.00	0.98±0.01
n = 0.0175	0.11±0.06	0.99±0.06	0.99±0.01	0.98±0.02
n = 0.0200	0.15±0.09	0.98±0.07	0.93±0.02	0.96±0.04

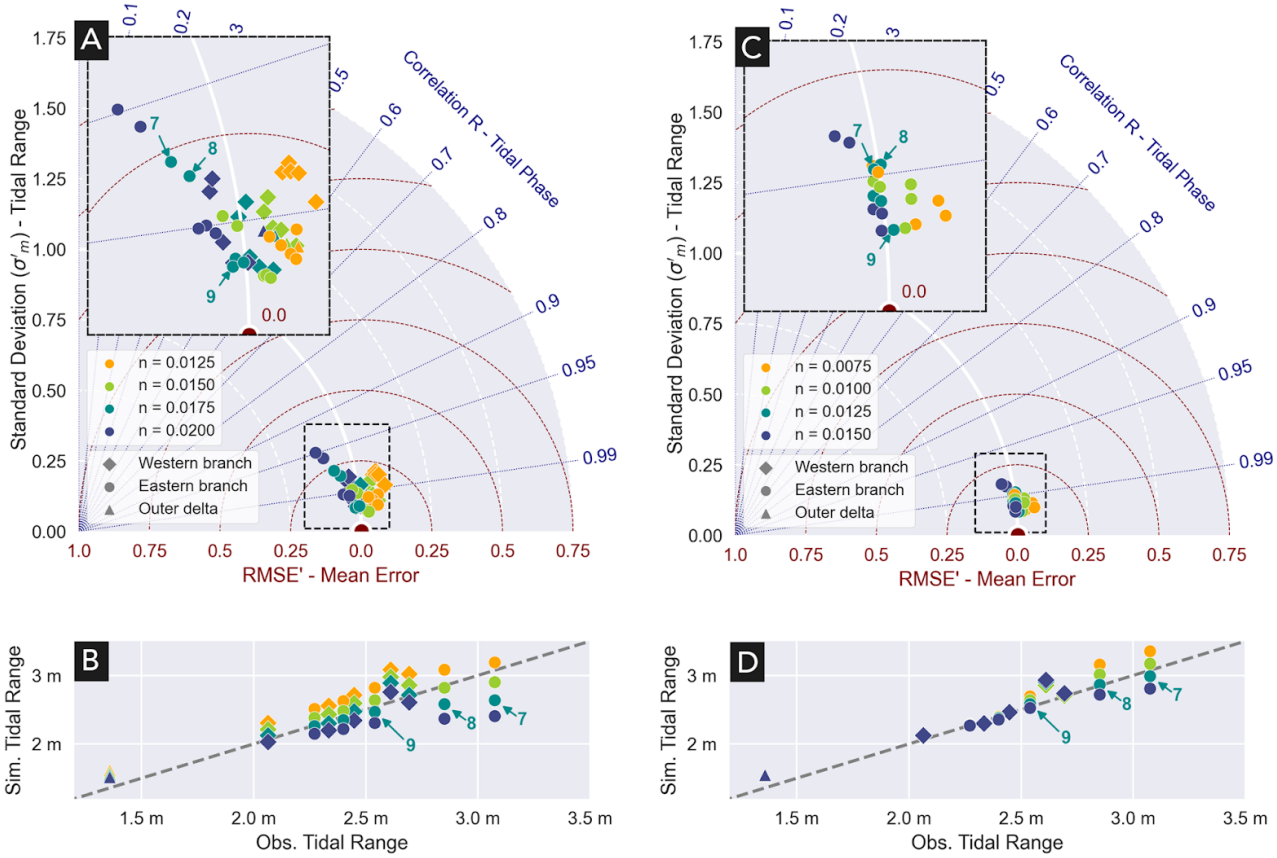

Figure S4 *| Normalised Taylor diagrams (A, C) representing the model performance and scatter plots of observed versus simulated tidal ranges (B, D) for different Manning coefficient values (color of markers) for (A, B) a single Manning coefficient for all branches (shape of marker) and (C, D) a different Manning coefficient value for the eastern branch compared to the western branch and outer delta.*

References

Bishop-Taylor, R., Sagar, S., Lymburner, L., Alam, I., Australia, J. S. G., Ave, C. J., & Drive, H. (2019). Sub-Pixel Waterline Extraction: Characterising Accuracy and Sensitivity to Indices and Spectra. *Remote Sensing*, *11*, 1–23. https://doi.org/10.3390/rs11242984

Ince, E. S., Barthelmes, F., Reißland, S., Elger, K., Förste, C., Flechtner, F., & Schuh, H. (2019). ICGEM – 15 years of successful collection and distribution of global gravitational models, associated services, and future plans. *Earth System Science Data*, *11*(2), 647–674. https://doi.org/10.5194/essd-11-647-2019

Kärnä, T., & Baptista, A. M. (2016). Evaluation of a long-term hindcast simulation for the Columbia River estuary. *Ocean Modelling*, *99*, 1–14. https://doi.org/10.1016/j.ocemod.2015.12.007

Khan, M. J. U., Ansary, M. N., Durand, F., Testut, L., Ishaque, M., Calmant, S., Krien, Y., Islam, A. K. M. S., & Papa, F. (2019). High-Resolution Intertidal Topography from Sentinel-2 Multi-Spectral Imagery: Synergy between Remote Sensing and Numerical Modeling. *Remote Sensing*, *11*(24), 2888. https://doi.org/10.3390/rs11242888

Mäkinen, J., & Ihde, J. (2008). Observing our Changing Earth. *International Association of Geodesy Symposia*, 81–87. https://doi.org/10.1007/978-3-540-85426-5_10

Sagar, S., Roberts, D., Bala, B., & Lymburner, L. (2017). Extracting the intertidal extent and topography of the Australian coastline from a 28 year time series of Landsat observations. *Remote Sensing of Environment*, *195*, 153–169. https://doi.org/10.1016/j.rse.2017.04.009

Zingerle, P., Pail, R., Gruber, T., & Oikonomidou, X. (2020). The combined global gravity field model XGM2019e. *Journal of Geodesy*, *94*(7), 66. https://doi.org/10.1007/s00190-020-01398-0